



# Egg protein derived ultralightweight hybrid monolithic aerogel for water purification

Sehmus Ozden<sup>1,2,3,4,\*</sup>, Susanna Monti<sup>5</sup>, Valentina Tozzini<sup>6,7</sup>, Nikita S. Dutta<sup>3</sup>, Stefania Gili<sup>8</sup>, Nick Caggiano<sup>2</sup>, A. James Link<sup>2</sup>, Nicola M. Pugno<sup>9,10</sup>, John Higgins<sup>8</sup>, Rodney D. Priestley<sup>1,2</sup>, Craig B. Arnold<sup>1,3,\*</sup>

<sup>1</sup> Princeton Institute for the Science and Technology of Materials, Princeton University, Princeton, NJ 08540, USA

<sup>2</sup> Chemical and Biological Engineering, Princeton University, Princeton, NJ 08540, USA

<sup>3</sup> Department of Mechanical and Aerospace Engineering, Princeton University, Princeton, NJ 08540, USA

<sup>4</sup> Aramco Americas, Aramco Research Center-Houston, 16300 Park Row, Houston, Texas, 77084, USA

<sup>5</sup> CNR-ICCOM, Institute of Chemistry of Organometallic Compounds, via G. Moruzzi 1, I-56124 Pisa, Italy

<sup>6</sup> Istituto Nanoscienze – Cnr, Piazza San Silvestro 12, 56127 Pisa, Italy

<sup>7</sup> NEST-Scuola Normale Superiore, Piazza San Silvestro 12, 56127 Pisa, Italy

<sup>8</sup> Department of Geosciences, Princeton University, Princeton, NJ 08540 USA

<sup>9</sup> Laboratory for Bioinspired, Bionic, Nano, Meta Materials and Mechanics, Department of Civil, Environmental and Mechanical Engineering, University of Trento, Italy

<sup>10</sup> School of Engineering and Materials Science, Queen Mary University of London, Mile End Road, London

The integration of 2D-graphitic carbon (G) with 1D-carbon nanofiber (CF) allows for the unique properties of 2D graphitic carbon to be combined with the low densities, mechanical performance, and high surface area required for applications across the energy and sustainability landscape. Through a combination of experiments and numerical modeling, we demonstrate the transformation of standard egg-white (EW) proteins into an ultralightweight G-CF aerogel with a multiscale structure. The resulting covalently-bonded hierarchical structure, derived from the complex underlying protein configuration, exhibits a density that is two orders of magnitude lower than existing state-of-the-art materials. We apply this material to the challenges of desalination and water purification, notably demonstrating that the G-CF aerogel significantly improves upon existing materials, capturing 98.2% of ionic impurities and 99.9% of nano/micropastic contamination from seawater.

**Keywords:** Hierarchical aerogel; Graphene; Carbon-fiber; Self-assembly; Classical molecular dynamics; Desalination; Water purification

## Introduction

Seamless covalent networks of 2D-Graphitic carbon (G) sheets and 1D carbon-nanofiber (CF) with hierarchical porosity have attracted interest for a wide range of engineering applications, including energy storage, water purification, catalysis, and

mechanical damping [1]. Their broad applicability arises from the theorized enhancement of properties like surface area, mechanical behavior, and electrochemical, electrical, and thermal conductivities [2–6], and to date, various methods such as templating or freeze-drying are used to fabricate such hierarchical porous carbon material systems [7–11]. However, while templating techniques have the advantage of generating hierarchical structures with tunable pore sizes and shapes, they also suffer from severe drawbacks, such as complicated post-template-

\* Corresponding authors.

E-mail addresses: Ozden, S. ([sehmosozden@gmail.com](mailto:sehmosozden@gmail.com)), Arnold, C.B. ([cbarnold@princeton.edu](mailto:cbarnold@princeton.edu)).

removal procedures that require additional resources and energy. Furthermore, previously reported works are related to interconnecting 2D-G and 1D-carbon nanotubes, while the seamlessly interconnected structure of 2D-G and 1D-CF has not been developed due to the challenges of processing and interface properties of G and CF. Therefore, developing novel, template-free approaches for manufacturing a greater variety of interconnected porous hybrids with complex hierarchical architectures is critically needed for a broad range of technological applications [7,12].

Modification of natural precursor materials offers new opportunities to achieve such structures and can provide clear advantages in terms of eco-friendliness and sustainability [13–15]. Proteins lend themselves particularly well to this purpose because of their intrinsic hierarchical structures, which stem from the self-organization of the primary sequence into systematic tertiary structures through the folding of the polypeptide chains [16,17]. There has been enormous effort to engineer the assembly of proteins to build various supramolecular architectures (e.g. fibrils, and scaffolds) by the rational design of protein–protein interactions and cross-linkers. However, there are few reports on processing these structures for constructing porous carbon-nanomaterials [17–21]. Exploiting the structural complexity and sustainability of natural materials to address advanced engineering needs in green manufacturing remains an area of great interest for a variety of materials applications.

In this work, we present the scalable fabrication of seamlessly interconnected, ultralightweight G and CF hierarchical aerogels by processing egg-white (EW) proteins without an external template and show its efficiency in water purification and desalination applications. We demonstrate that EW-proteins that consist of  $\alpha$ -helix and  $\beta$ -sheets transform from their secondary structure to amyloid-type  $\beta$ -sheet components during the pyrolysis process. These intermolecular  $\beta$ -sheets lead to the formation of a hierarchical aerogel consisting of a covalently-bonded G-CF network with porosity at both the nano- and microscales. We achieve a density of  $0.0038 \pm 0.0006 \text{ g/cm}^3$ , two orders of magnitude lower than the reported density for other graphene aerogels [11,23]. To understand the formation mechanism and transformation of the protein structures into the final architectures, atomistic reactive molecular dynamics (MD) simulations are used in conjunction with the experiments. Such complex materials with hierarchical two-level pore structures have a broad range of applications. Here, we demonstrate that the G-CF aerogel can be used for the desalination of seawater with 98.2% efficiency and 99.995% microplastic purification exceeding current state-of-the-art materials [22].

## Results and discussion

Covalently interconnected G-CF aerogels with two-level porosity at the nanoscale and microscale are fabricated by freeze-drying followed by pyrolysis at 900 °C under  $\text{N}_2$  atmosphere (Fig. 1). The EW-proteins used in this study are obtained from standard consumer products and as such contain several different types of proteins. As a control, we have applied the same protocol to pure proteins with different structures—namely, Ovalbumin (OVA), Bovine Serum Albumin (BSA), and Collagen Gelatin

(CG)—to understand the role of protein structure on the formation of the G-CF aerogel network. While OVA and BSA consist of both  $\alpha$ -helices and  $\beta$ -sheets with different structures, CG is made of  $\alpha$ -helices with triple helices (Fig. S1). In spite of the different molecular organization, the results after freeze-drying and pyrolysis treatments of BSA and OVA are similar to that of EW-proteins—micro-sized large graphitic carbon sheets seamlessly interconnected with CF via covalent bonding. Conversely, in the case of CG, the structure is dominated by micro-sized CF (Fig. S1), while there are partial 2D-graphitic carbon sheets and a G-CF seamless network. The hierarchical G-CF aerogel obtained with EW is ultralightweight with a density of  $0.0038 \pm 0.0006 \text{ g/cm}^3$ . Compared to the class of graphene nanoporous materials, the density is two orders of magnitude smaller [11,23].

To gain further insight into the morphology of G-CF aerogels made of EW-proteins, the surface and internal structure are imaged using scanning electron microscopy (SEM). Fig. 1b–d show the surface view of the hierarchically structured G-CF aerogel displaying a rather flat surface, consisting of G-sheets, seamlessly interconnected with CF defining a micrometer-sized structure of adjacent pores. In order to understand the in-depth morphology of the G-CF aerogel, the block is sectioned, and the cross-section structure is imaged using SEM (Fig. 1e–g). The architecture of the G-CF aerogel entirely consists of porous cages made of G-sheets seamlessly stitched with CF. Conversely, the inner structure of the CG derived structure obtained with the same treatment appear composed of elongated fibers and fibrils with micron-scale diameter and a small amount of G-sheets (Fig. S1c). This difference stems from the supramolecular organization of the precursors, already in the pre-pyrolysis phase, due to CG having its own particular fiber organization [24,25].

Detailed high-resolution transmission electron microscopy (HRTEM) is performed to elucidate the material nanostructure. HRTEM with diffraction analysis shows that the G structure is polycrystalline (Fig. 2a). The G-structure contains hexagonal lattices with various defect structures such as single-point defects and vacancy defects, which may be considered nanopores (Fig. 2b). Intensity analysis of the TEM micrograph displays a periodicity of  $\sim 2.5 \text{ \AA}$ , compatible with that of the theoretical value of the hexagonal lattice ( $2.6 \text{ \AA}$ ) (Fig. 2c). The HRTEM of interconnected G and CF is shown in Fig. 2d. HRTEM of CF reveals that it consists of interconnected graphitic structures with high levels of defects (Fig. 2e). Additionally, an interface region is observed where structural defects are present in large numbers (Fig. 2f). The average pore size distribution of G-CF aerogel network is around 4 nm, which is mostly coming from defects of CF and the interface connection between G and CF (Figs. S2 and S7). In addition, double porous structure of the G-CF is an excellent pore structure of 3D architecture with a high packing density.

The formation of G-CF structures is confirmed by spectroscopic characterization. Raman spectra of carbon materials typically have two characteristic peaks, G-band and D-band, which are related to the  $\text{sp}^2$  and  $\text{sp}^3$ -carbon, respectively (Fig. 2g). In particular, the G-band confirms the presence of  $\text{sp}^2$ -carbon, while the D bands indicate the presence of  $\text{sp}^3$ -carbon as a result of defects in the hexagonal lattice of the graphitic carbon. The Raman spectra of the G-sheets and CF are measured separately

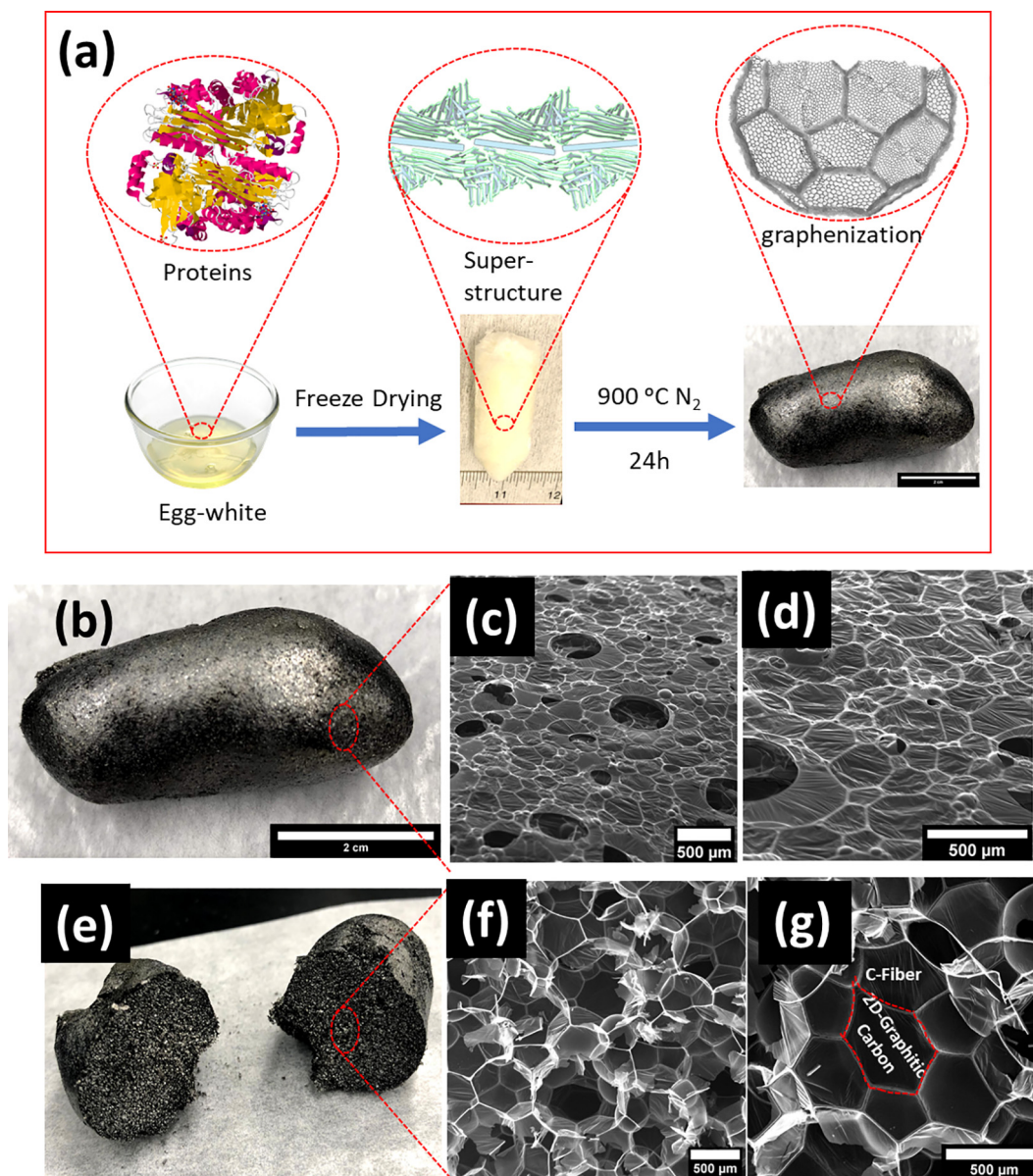


FIGURE 1

(a) Schematic synthesis illustration of the hierarchical monolith of graphitic carbon and carbon fiber (G-CF) aerogel network, (b) picture of ultralightweight multifunctional G-CF aerogel, (c, d) SEM images of the G-CF aerogel surface and (e) inner picture of ultralightweight G-CF aerogel (f, g). SEM images of the porous inner structure of the G-CF aerogel consist of buckyball-like cages.

(Fig. 2g). Both structures display the two bands at  $1348\text{ cm}^{-1}$  and  $1591\text{ cm}^{-1}$ , respectively. The relative defect density can be determined from the ratio between the D-band and G-band intensities,  $I_D:I_G$ . Here, it is found that the  $I_D:I_G$  ratio in the CF ( $I_D:I_G = 1.01$ ) is larger than in the G-sheet ( $I_D:I_G = 0.89$ ), confirming the HRTEM observation of a higher content of defects in the CF-structure. The X-ray diffraction (XRD) pattern of the pyrolyzed EW-proteins shows two peaks at  $13.9^\circ$  and  $25.5^\circ$  that correspond to oxygenated and N-doped graphitic carbon, respectively (Fig. 2h). The composition of the G-CF aerogel consists of 94.9% carbon, 4.08% oxygen, and 1.02% nitrogen atoms (Fig. S3). In high-resolution XPS characterization, the C–C, C–O/C–N, C=O/C=N and  $\pi$ - $\pi$  bond peaks are around 284.6 eV, 286.2 eV, 287.4 eV, and 289.2 eV, respectively. Fitting

the N1s peak corresponds to pyridinic, pyrrolic, and N-doped graphitic structures at 398.2 eV, 399.6 eV, and 401.4 eV, respectively (Fig. 2i-j) [26].

To understand the formation of the hierarchical complex structure of the G-CF aerogel and the evolution of the protein assemblies during freeze-drying and pyrolysis, microscopic and spectroscopic characterizations with the aid of MD-simulations are performed. The protein structures are self-assembled after freeze-drying, and the morphology of the self-assembled proteins does not change much at 200 °C. Between 200 °C and 400 °C, we observe a macroscopic structural reorganization and the formation of the micro-scale porous cells, whose macroscopic conformation remains unchanged at higher temperatures. We infer that in this phase, a supramolecular-level reorganization occurs,

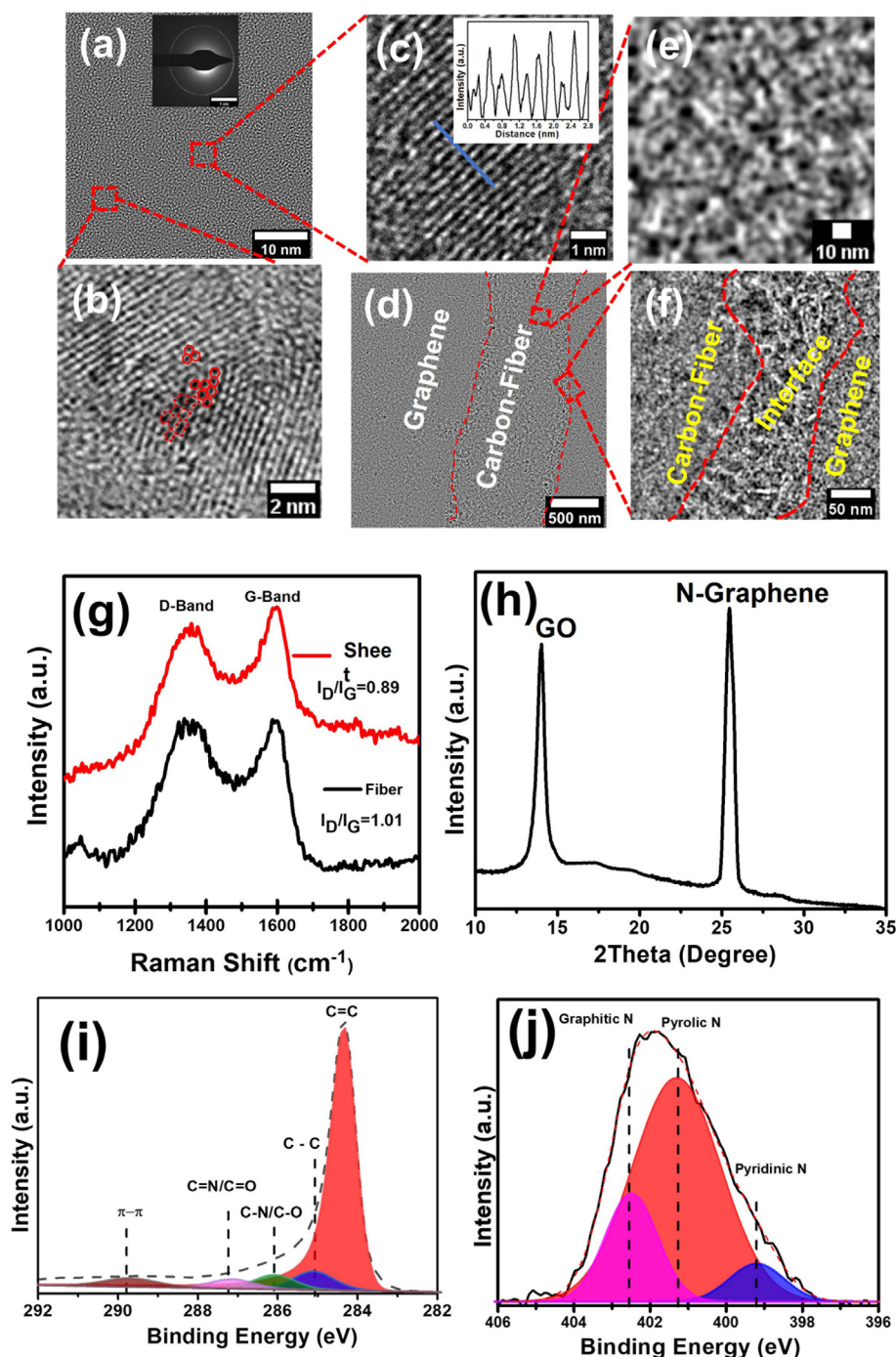


FIGURE 2

(a–c) HRTEM image of G-sheet with inset diffraction pattern showing polycrystalline structure of G-sheet, marked structural defects, and inset intensity analysis, (d, e) HRTEM image of CF structure, (f) interface connection of G-sheet and CF structure, (g) Raman spectra of G-layers, and CF, (h) XRD of hierarchical G-CF aerogels, (i) C1s and (j) N1s XPS spectra of G-CF aerogel.

corresponding to an increase of the amyloid content and the formation of extended amyloid structures, and after 400 °C, crystallization of the system takes place.

Reactive MD-simulations allow us to further understand the formation mechanism and transformation of the protein structures into the final architecture. We consider three models: (i) a single extended  $\beta$ -sheet, (ii) stacked  $\beta$ -sheets, and (iii) collagen-fibers (Fig. 3 and Fig. S4) (Model iii discussed in Fig. S8). The

rationale behind the building of models (i) and (ii) is the fact that both OVA and BSA undergo amyloid-type aggregation, and the formation of large portions of  $\beta$ -sheets [27,28]. We first simulate the heating of model (i) (Fig. 3b) and observe a fast release of molecular hydrogen, water, and hydronium ions already in the early heating phases. The reaction mechanism takes advantage of the  $\beta$ -sheet hydrogen-bonds network cross-linking the protein backbones. The parallel strands structure inherited from the  $\beta$ -

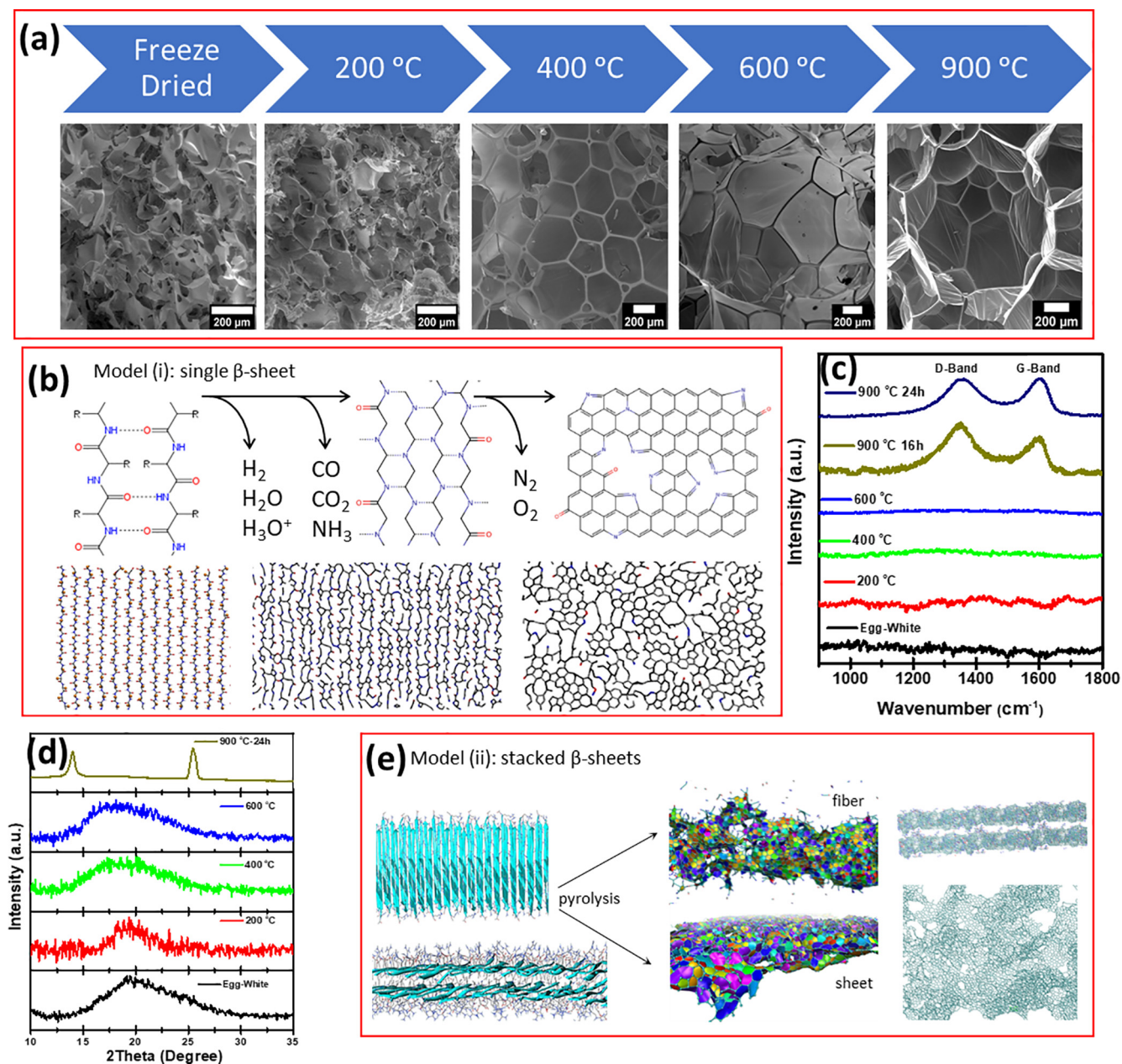


FIGURE 3

Evolution of the hierarchical G-CF structure during the process. (a) Microscopic images of the EW proteins transform at different temperatures, (b) simulation of heating and pyrolysis of the  $\beta$ -sheet model, (c) the Raman spectra of EW in the D and G band region at different temperatures, (d) the XRD spectra of EW protein transformation at different temperatures and (e) simulation of pyrolysis of the stacked sheet model (ii) for the formation of G and CF.

sheets is still clearly visible, though the residual polypeptidic backbones are interconnected at many points. The formation of the graphitic carbon network occurs at higher temperature through cross-linking and interconnection of the protein backbones. The phases of the process are illustrated using simulations of the model (i) in Fig. 3b by means of schematic and molecular representations and paired to the corresponding microscopic images in Fig. 3a and Figs. S5-S6.

The spectroscopic characterization of the process supports the mechanism proposed by the MD-simulations (Fig. 3c-d). The characteristic D-band and G-band of the graphitic structures in Raman spectroscopy are not observed from self-assembled pro-

tein structures that have been heat-treated 200 °C, 400 °C, and 600 °C. The characteristic D-band and G-band is observed from the protein assembly pyrolyzed at 900 °C for 16 h and further (Fig. 3c). The crystal structures are also analyzed by XRD. As is seen in Fig. 3d, the self-assembled protein structures and pyrolyzed structures at 200 °C, 400 °C, and 600 °C show an amorphous carbon structure. A crystalline structure that shows oxidized G and N-doped G-CF is observed with pyrolyzation at 900 °C for 24 h.

We then address the question of the formation of CF and G-sheets in EW/OVA. It is known that these stem from the supramolecular aggregation form with different boundary condi-

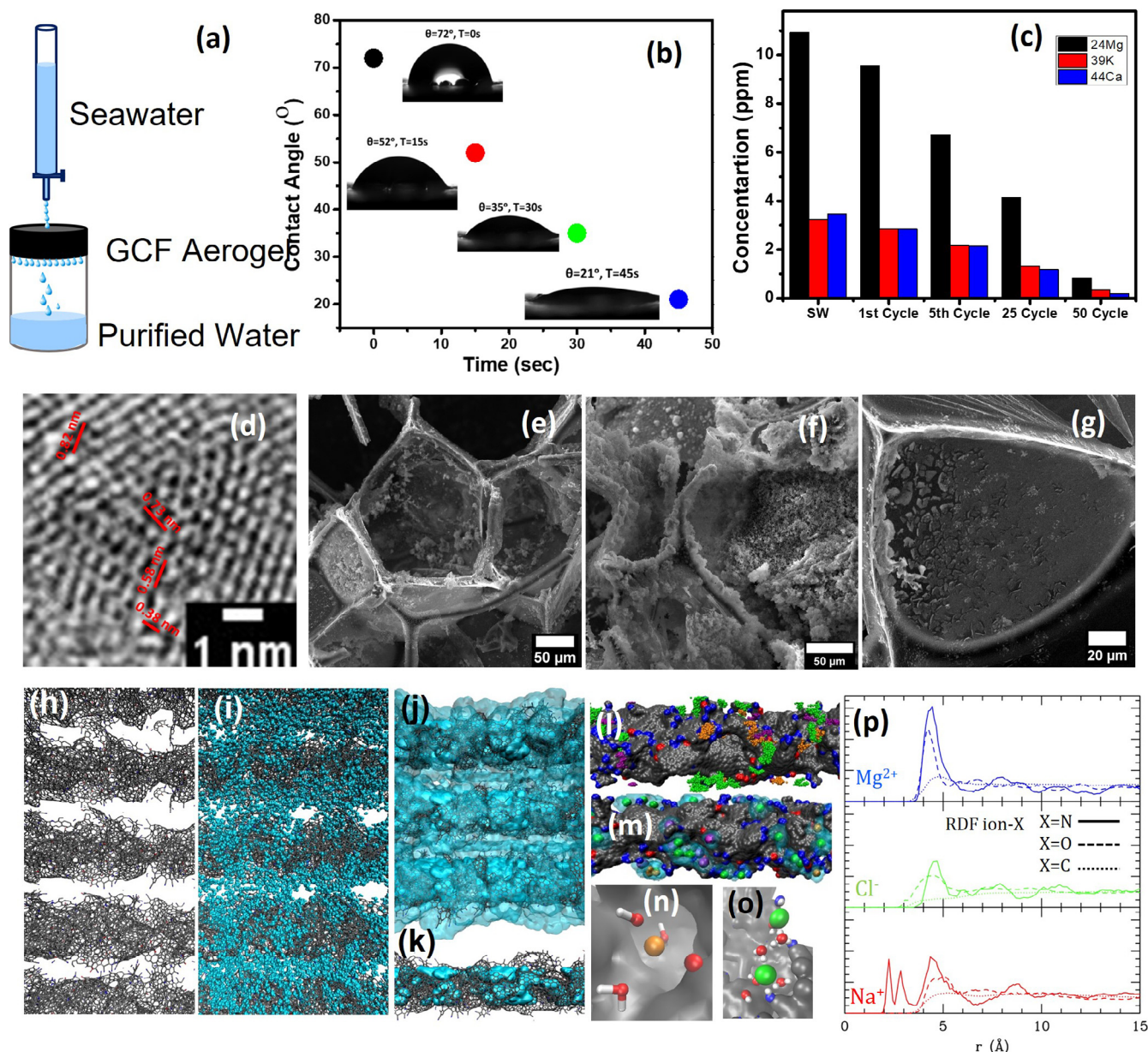


FIGURE 4

(a) Schematic representation of the seawater desalination device, (b) measurement of the contact angle as a function of time for a droplet on the G-CF surface, (c) measurement of the salt concentration as a function of the cycles, (d) percentage of PS nano/microplastics removed from water by EW-aerogels and AC, (e) TEM image of the nanoporous 2D graphitic-carbon sheet, (f-g) structure of the G-CF after 50 cycles of seawater desalination, (h) model for the nanofibers matrix. Water flowing (i) through the nanochannels (water molecules in blue), (j) in the interstitials (represented as isodensity transparent surfaces), and (k) within the fiber (as opaque isodensity surface), (l-m) the ions trapped on the fiber (chlorine in green, sodium in orange, magnesium in violet; nitrogen and oxygen in the fiber are in blue and red), (n-o) same as previous, but the hydration shell of the ions is represented through a transparent isosurface, (p) radial distribution functions of the ion-fiber atom pairs. Ion type are coded in colors as reported, while the fiber atoms as lines as reported.

tions (e.g. isotropic or anisotropic tension of the structure) [27]. In order to simulate these different conditions in the reduced model systems, we have produced model systems for CF and G-sheets by stacking of  $\beta$ -sheets (model (ii), Fig. 3e). With 2–4 sheets stacked, a thickness of 5–10 nm is obtained. From (ii) we obtained the sheet geometry by extending the simulation supercell by periodicity in the two in-plane directions, while the fiber geometry is obtained extending in only one direction (Fig. S4). These two different boundary conditions mimic the isotropic and anisotropic superficial strains that originate in sheets and fibers, respectively.

We simulate the pyrolysis of these two systems and obtain the formation of nano-sized pores, clearly visible in the final configuration of the G-sheet (Fig. 3e and Fig. S7) and somewhat smaller in the fiber-structures. Pores form because of the large amount of gases released during the process, which desorb from the surfaces of the sheets and fibers and fill the micro-bubbles, contributing to enlarging and stabilizing them, but at the same time creating voids at nanoscale. In agreement with the HRTEM observations, the superficial graphenized structure of the model sheet after pyrolysis (graphenized parts are represented as colored hexagons and pentagons) is somewhat more ordered than that of the fiber,

although not as ordered as the experimental one, which is in turn more similar to that obtained in the single sheet simulated pyrolysis. This slight discrepancy between simulation and experiment is essentially due to the supercell size and heating time, which could not be tuned to the experimental counterparts. Thus, in the simulations, only small ordered domains are observed (Figs. S7-S8).

The 2D-graphitic carbon and carbon-fiber based aerogels have a broad range of promising applications [2–7]. State-of-the-art water purification and desalination demands the development of green and inexpensive novel materials and technologies with specific porosity [22,29]. There are various reports of processed natural materials for water desalination and purification via thermal and capacitive deionization (CDI), but they require energy input [30,31]. Here, we demonstrate the G-CF aerogel for water desalination and purification. The G-CF aerogel (5 mm thickness) is placed over the mouth of a funnel, and seawater (from the New Jersey shore) is allowed to pass through it at a 0.5 ml/min flow rate by gravity (Fig. 4a). The fast water adsorption, demonstrated by the decrease of the contact angle of the water droplet on the G-CF surface, is due to capillarity enhanced by the interaction of water with charged defects of the nanoporous matrix (Fig. 4b). Seawater is passed through the G-CF aerogel in 50 cycles, and the filtered seawater is analyzed by inductively coupled-plasma mass-spectrometry (ICP-MS) (Fig. 4c). On the first cycle of seawater purification, 13.1% of  $Mg^{2+}$ , 13.6% of  $K^+$ , and 17.9%  $Ca^{2+}$  ions are rejected from the seawater. The ratio of salt ions decreases with increased purification cycles. At the end of 50 purification cycles, 92%  $Mg^{2+}$ , 90.1%  $K^+$ , and 94%  $Ca^{2+}$  ions are rejected. Conductivity and pH tests also show that the seawater is highly purified (Fig. S9). The adsorption capacity of the G-CF aerogel is calculated by measuring the weight change before and after the water filtration (samples were dried overnight at 100 °C). The salt adsorption capacity of G-CF aerogels is  $\sim 32.6$  g/g (Figs. S10d- and S11). The salt adsorption capacity of G-CF aerogels is above the average reports in the literature (Fig. 5a) [32–38].

In another demonstration we have shown that the G-CF aerogel is effective for removing nano/micro plastics from water since nano/micro-plastic contamination in seawater is one of the major environmental issues. So far, studies mainly are focused on contamination by microplastics, and less attention is given to nanoplastics. The environmental impact of nanoplastics is expected to be different from microplastics because of their high surface area ratio that results strong adsorption with contaminants in seawater such as heavy metals. Here,  $\sim 147$  nm (2.72 mg/ml) and  $\sim 400$  nm (13.32 mg/ml) polystyrene (PS) microplastics contaminated water samples are prepared and purified by the same setup as the seawater desalination above. In the first cycle of purification, 93.2% ( $\sim 147$  nm), and 98.5% ( $\sim 400$  nm) of PS-nanoparticles, respectively, are removed from water using EW-Aerogels (Fig. 4d). After 15 cycles, the removal levels off to 99.986% of  $\sim 147$  nm and 99.995% of  $\sim 400$  nm size PS-nanoparticles, respectively, being removed from water (Fig. 4d and S10). For comparison, we have repeated the same experiment using activated-carbon (AC). In this case, after the first-cycle 82.4% of PS-nanoparticles ( $\sim 147$  nm) are removed, and after the 15th-cycle the total removal asymptotes to 98.2%, which is similar to current state of the art materials [22]. We attribute the improvement in microplastic removal with the G-CF-aerogel to the specific adsorption mechanism in our material in which strong non-covalent interactions (e.g.  $\pi$ - $\pi$ ) exist between PS-nanoparticles and the G-CF surface. Furthermore, the hierarchically organized multiscale porous structure of G-CF acts as an effective trap to adsorb nano/microplastic on the large surface, and thus G-CF is more effective than AC at removing microplastics. In addition, mass driving force is another effective mechanism for the diffusion of PS nano/micro plastics from the solution to the G-CF aerogels surface.

While the benefits of the G-CF aerogel for purification applications include its mechanical stability, low-cost, and durability, the key property enabling its efficacy is the double-level hierarchical porosity. The micron-level porosity allows water to quickly penetrate into the structure and selects possibly present

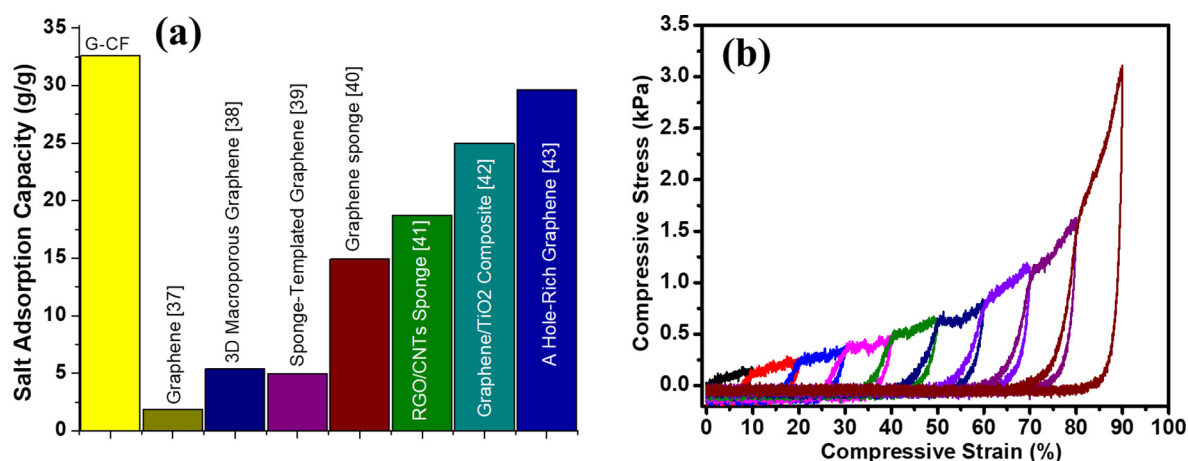


**FIGURE 5**

(a) The comparison for salt adsorption capacity of G-CF aerogels with some reported carbon-based materials and (b) compressive load-unload curve of EW-aerogel from 10% to 90% strain.

macroscopic pollutant particles from seawater (Fig. S11), while the nanoporosity acts as a salt filter. The desalination is hypothesized to be made more efficient by the O- and N-residual functional groups residing on the nano-sized pores and defects in Fig. 4e, acting as traps for the ions [39,40]. This effect is likely to be enhanced by a system of nano-channels present in the G-sheets-CF-matrix, which additionally improves the separation of the ions and larger particles due to the double-level porosity, while the aerogel structure favors the water adsorption ensuring at the same time large structural stability against swelling. The final result is purified and desalinated water. The SEM images of G-CF aerogel after seawater pass through show that a layer of salt and other impurities is deposited on the surface of the aerogel (Fig. 4e–g).

In order to gain insight into the ion-filtering mechanism at the molecular-level, we performed MD-simulations of a nanoporous fiber taken from simulations of Fig. 3e, periodically repeated to mimic the structure of nano-channels forming within the nano-fiber-matrix, and completely hydrated and with Na<sup>+</sup>, Mg<sup>2+</sup> and Cl<sup>-</sup> ions concentrations as in seawater (Fig. 4h). As shown in Fig. 4i, j, water penetrates through the interstitials of the porous carbon structure, as expected; interestingly, however, it also fills the nano-sized pores easily within the fiber itself (Fig. 4k). While water mobility is high, ions are clearly trapped on the surface or within cavities of the carbon-fiber, as shown by Fig. 4l. Ions show a preferential accumulation near the sites occupied by N or O functionalities (blue and red areas, respectively). This preference is confirmed by the radial distribution functions (RDF) shown in Fig. 4m: while the RDF of the ions with C (dotted lines) is relatively flat, the RDF of ions with N (solid lines) and with O (dashed lines) display well-marked coordination peaks, indicating that their complexes with the N and O functional sites on the fiber are stable. To clarify the molecular interaction mechanism, we first observe that the ions, which usually have full water coordination shells when in solution, are only partially hydrated when trapped on the fiber (Fig. 4n). There are important differences between the RDFs of different ions due to the different behavior of their coordination shells: sodium has two peaks at very short distances because the carbonyl O in the fiber is capable of replacing one of the oxygen of its hydration shell (Fig. 4o). This is not possible with magnesium and especially with chlorine, whose direct coordination is with H of water. Conversely, Cl<sup>-</sup> can be coordinated to the hydrogen of NH groups, occasionally protonated in the fiber, which explains its ability to reach the shorter distance to N. The trapping mechanism is an effect of the mediation of water molecules between the ion and the C and N sites in the fiber, rather than an electrostatic effect (Figs. S12–S13).

The mechanical properties of water desalination and purification materials is critical not only for their design, also for understanding their failure mechanisms, including the surface damage, mechanical and chemical aging, delamination, and loss of dimensional stability of the structures [2,8,44–47]. In addition to good chemical and fouling resistances, materials for water desalination and purification require high mechanical stability and durability. Fig. 5b shows the load-unload compressive stress–strain curve of G-CF structure made out of the fresh egg-white. The compression loading curve indicate that the G-CF

aerogel can be compressed down to about 90% strain. As the load of the aerogel increases, the nature of the curve remains same during loading–unloading test. The compression stress of the G-CF aerogel is ~3.1 Mpa, which can indicate that the graphitic carbon and carbon-fiber in the G-CF aerogel is seamlessly interconnected [2,8].

## Conclusions

We have developed a scalable, green approach based on self-assembly of protein structures to create a seamlessly connected hybrid G-CF aerogel network. This is the first time such seamlessly interconnected, ultralightweight 2D-graphitic carbon and carbon-fiber aerogels with hierarchical architecture is reported. The architecture of the G-CF aerogel entirely consists of porous cages made of graphitic carbon sheets that are seamlessly stitched with CF. The obtained G-CF aerogel is ultralightweight ( $0.0038 \pm 0.0006 \text{ g/cm}^3$ ), yet with a mechanically stable and resistant hierarchical architecture that entirely consists of porous cells. Reactive MD-simulations at the atomic scale help explain the assembly mechanisms of the proteins and the phase transformations which enable the interconnected G-CF aerogel to form. We have shown that protein chains adopt a tighter arrangement, alter their structure, orientation, and shape, and start to interact more strongly with each other, making covalent connections during the pyrolysis process at high temperature. The hierarchical G-CF displays two distinct levels of porosity at both the micro- and nano-scales, which is highly advantageous for desalination and microplastic purification of sea water. Moreover, chemical interconnection between graphitic carbon and CF structures gives a large structural stability against swelling of the G-CF aerogels that makes the desalination and purification efficiency consistent. Indeed, we have demonstrated that the G-CF aerogel desalinates seawater with 98.2% efficiency and extracts microplastics from water with 99.995% efficiency. The method we have developed offers an excellent opportunity for creating template-free multifunctional hierarchical porous materials for critically needed applications.

## Experimental

To prepare hierarchically interconnected 2D-graphitic carbon and 1D-carbon-fiber aerogel, egg white (EW) extracted from cage-free unpasteurized eggs is first freeze-dried and then pyrolyzed at 900 °C under N<sub>2</sub>. In addition to the EW-proteins, pure ovalbumin from chicken eggs (Sigma Aldrich), bovine-serum-albumin derived from cows (Sigma Aldrich), and gelatin proteins derived from bovine skin (Sigma Aldrich) are dissolved in DI-water (0.5 mg/ml) followed by freeze-drying and pyrolyzation at 900 °C under N<sub>2</sub>.

The chemical composition of aerogels is measured by scanning electron microscopy (SEM) (FEI Quanta 200 FEG ESEM) and transmission electron microscopy (Talos F200X Scanning/Transmission Electron Microscope (S/TEM)). X-ray diffraction (XRD) characterization is performed using a Bruker D8 Discover X-ray Diffractometer. X-ray photoelectron spectroscopy (XPS) characterization is carried out using Thermo Fisher K-Alpha + X-ray Photoelectron Spectrometer (XPS/UPS). The salt concentration in water is measured by inductively coupled



plasma mass spectrometry (ICP-MS). Nitrogen adsorption–desorption isotherms and pore size distributions of the aerogels were measured at 77 K in powder form by Brunauer-Emmett-Teller (BET). Raman spectroscopy analysis is collected using a Horiba Raman spectrometer with a 532 nm wavelength laser. A piece of the G-CF sample is placed on a microscope slide and mounted on the optical microscope stage. To measure the Raman spectra of 2D-graphitic carbon layer and carbon-fiber regions, we focused to these two structures separately with the optical microscope camera, and performed the Raman measurement using 532 nm wavelength light.

## Simulation

The process of dehydration-pyrolysis is simulated by means of classical molecular dynamics, using the reactive force field ReaxFF (ADF/ReaxFF software [41,42]), using previously tested parameters [43]. The system configurations are collected every 0.1 ps. Temperature and pressure were regulated through the Berendsen thermostat and barostat with relaxation constants of 0.1 ps, and the time step is set to 0.2 fs. For the other simulations (equilibration, structure optimization, hydrated fiber simulation) we use the AMBER package (ff99SB force field) [27]. The simulations supercells sizes used were various, depending on the model system, in the range 50–200 Å (details in the SI). The starting configuration for simulations were prepared on the basis of the amyloid super-molecular organization for the EW/OVA/BSA models, which were consequently built using as a reference atomistic model the  $\beta$ -sheet formed by the  $\beta$ -RADA-16-I self-assembling peptide. For the Gel model, we used the bovine collagen fibril model structure. Further details of the simulation procedure and analysis are reported in the [Supporting Information](#).

## Author contributions

S.O. and C.B.A. originated the project ideas, and S.O. performed the experiments. S.O., C.B.A and R.D.P. coordinated the project. S.M., V.T. and N.M.P. performed reactive molecular dynamic simulations and wrote the relevant discussion. N.S.D. conducted TEM characterization. S.G. and J.H. performed ICP-MS. N.C. conducted freeze-drying process. S.O., C.B.A and R.D.P. wrote the manuscript. All the authors discussed the results and commented on the manuscript.

## Declaration of Competing Interest

The authors declare that they have no known competing financial interests or personal relationships that could have appeared to influence the work reported in this paper.

## Acknowledgements

S.O. acknowledges financial support from the Princeton Center for Complex Materials (PCCM) Postdoctoral Fellowship. The authors acknowledge the use of Princeton's Imaging and Analysis Center, which is partially supported through the Princeton Center for Complex Materials (PCCM), a National Science Foundation (NSF)-MRSEC program (DMR2011750). Authors are grateful to Douglas M. Scott for providing polystyrene nanoparticles.

## Appendix A. Supplementary data

Supplementary data to this article can be found online at <https://doi.org/10.1016/j.mattod.2022.08.001>.

## References

- [1] P.S. Owuor et al., *Oxford Open Mater. Sci.* 1 (2021) 1–19, <https://doi.org/10.1093/oxfmat/itab004>.
- [2] S. Ozden et al., *Adv. Mater.* 11 (2015) 1842, <https://doi.org/10.1002/adma.201404995>.
- [3] Z. Gao et al., *Science* 6 (2020) 1–11, <https://doi.org/10.1126/sciadv.aaz4191>.
- [4] F.J. Martin-Martinez et al., *ACS Nano* 12 (8) (2018) 7425–7433, <https://doi.org/10.1021/acsnano.8b04379>.
- [5] Y. Zhu et al., *Nat. Commun.* 3 (2012) 1225–1232, <https://doi.org/10.1038/ncomms2234>.
- [6] N. Gupta et al., *ACS Nano* 15 (2021) 1342–1350, <https://doi.org/10.1021/acsnano.0c08588>.
- [7] X.Y. Yang et al., *Chem. Commun.* 47 (2011) 2763–2786, <https://doi.org/10.1039/C0CC03734F>.
- [8] S. Vinod et al., *Nat. Commun.* 5 (2014) 4541, <https://doi.org/10.1038/ncomms5541>.
- [9] L. Wu et al., *Natl. Sci. Rev.* 11 (2020) 1667–1701, <https://doi.org/10.1093/nsr/nwaa183>.
- [10] C. Lee et al., *Chem. Sus. Chem.* 11 (2018) 2960–2966, <https://doi.org/10.1002/cssc.201800982>.
- [11] Z. Sun et al., *Chem. Rev.* 120 (2020) 10336–10453, <https://doi.org/10.1021/acs.chemrev.0c00083>.
- [12] Q. Wang et al., *Nano Today* 36 (2021) 101033, <https://doi.org/10.1016/j.nantod.2020.101033>.
- [13] F. Jehle et al., *ACS Nano* 12 (2018) 2160–2168, <https://doi.org/10.1021/acsnano.7b07905>.
- [14] T.P.J. Knowles et al., *Nat. Nano.* 5 (2010) 3–6, <https://doi.org/10.1038/nnano.2010.26>.
- [15] H. Sun et al., *Nano Today* 14 (2017) 16–41, <https://doi.org/10.1016/j.nantod.2017.04.006>.
- [16] Q. Luo et al., *Chem. Rev.* 116 (2016) 13571–13632, <https://doi.org/10.1021/acs.chemrev.6b00228>.
- [17] K. Matsuura, *RSC Adv.* 4 (2014) 2942–2953, <https://doi.org/10.1039/C3RA45944F>.
- [18] S. Elsharkawy et al., *Nat. Commun.* 9 (2018) 1–12, <https://doi.org/10.1038/s41467-018-04319-0>.
- [19] S.-Y. Cho et al., *Nat. Commun.* 6 (2015) 1–7, <https://doi.org/10.1038/ncomms8145>.
- [20] P. Katyal et al., *ACS Biomater. Sci. Eng.* 5 (2019) 4132–4147, <https://doi.org/10.1021/acsbiomaterials.9b00408>.
- [21] M. Heim et al., *Chem. Soc. Rev.* 39 (2010) 156–164, <https://doi.org/10.1039/B813273A>.
- [22] M. Lapointe et al., *Environ. Sci. Technol.* 54 (2020) 8719–8727, <https://doi.org/10.1021/acs.est.0c00712>.
- [23] A. Klechikov et al., *Chem. Commun.* 51 (2015) 15280–15283, <https://doi.org/10.1039/C5CC05474E>.
- [24] L.E.R.O. Leary et al., *Nat. Chem.* 3 (2011) 821–828, <https://doi.org/10.1038/nchem.1123>.
- [25] W. Zhang et al., *Chem. Mater.* 15 (2003) 3221–3226, <https://doi.org/10.1021/cm030080g>.
- [26] S. Ozden, *Et. al. Nanoscale* 11 (2019) 12489–12496, <https://doi.org/10.1039/C9NR01321K>.
- [27] K.J.A. Jansens et al., *ACS Omega* 2 (2017) 4612–4620, <https://doi.org/10.1021/acsomega.7b00366>.
- [28] N.K. Holm et al., *Acta - Proteins Prot.* 1774 (2007) 1128–1138, <https://doi.org/10.1016/j.bbapap.2007.06.008>.
- [29] J.J. Patil et al., *J. Mater. Chem.* 9 (2021) 3270–3289, <https://doi.org/10.1039/D0TA08928A>.
- [30] Hou et al., *Sci. Adv.* 5 (2019) 1–9, <https://doi.org/10.1126/sciadv.aaw3203>.
- [31] A.R. Wood et al., *RSC Adv.* 11 (2021) 9628, <https://doi.org/10.1039/D0RA10763H>.
- [32] H. Li et al., *J. Mater. Chem.* 19 (2009) 6773–6779, <https://doi.org/10.1039/B907703K>.
- [33] H. Wang et al., *J. Mater. Chem. A* 1 (2013) 11778–11789, <https://doi.org/10.1039/C3TA11926B>.
- [34] Z.Y. Yang et al., *Adv. Funct. Mater.* 24 (2014) 3917–3925, <https://doi.org/10.1002/adfm.201304091>.

- [35] X. Xu et al., *Sci. Rep.* 5 (2015) 8458, <https://doi.org/10.1038/srep08458>.
- [36] X. Xu et al., *J. Mater. Chem. A* 3 (2015) 13418–13425, <https://doi.org/10.1039/C5TA01889G>.
- [37] H. Yin et al., *Adv. Mater.* 25 (2013) 6270–6276, <https://doi.org/10.1002/adma.201302223>.
- [38] J. Li et al., *Carbon* 129 (2018) 95–103, <https://doi.org/10.1016/j.carbon.2017.11.095>.
- [39] T.E. Culp et al., *Science* 75 (2021) 72–75, <https://doi.org/10.1126/science.abb8518>.
- [40] A. Boretti et al., *npj Clean Water* (2018) 1–11, <https://doi.org/10.1038/s41545-018-0004-z>.
- [41] J. Park et al., *Biophys. J.* 90 (2006) 2510–2524, <https://doi.org/10.1529/biophysj.105.074906>.
- [42] S. Monti, *J. Phys. Chem. C* 111 (2007) 16962–16973, <https://doi.org/10.1021/jp075154g>.
- [43] H. Azakami et al., *Agric. Food Chem.* 53 (2005) 1254–1257, <https://doi.org/10.1021/jf049325f>.
- [44] K. Wang et al., *Desalination* 401 (2017) 190–205, <https://doi.org/10.1016/j.desal.2016.06.032>.
- [45] S. Dervin et al., *Nanoscale* 8 (2016) 15115–15131, <https://doi.org/10.1039/C6NR04508A>.
- [46] P.S. Owour et al., *Adv. Mater. Interfaces* 4 (2017) 1700030, <https://doi.org/10.1002/admi.201700030>.
- [47] S. Vinod et al., *Nanoscale* 8 (2016) 15857–15863, <https://doi.org/10.1039/C6NR04252J>.